UCLouvain

epl

École polytechnique de Louvain

# Calibration of SKA-low antenna array using drones

## Load impedance and ground effect on calibration

Author: **Corentin Schovaers**
Supervisors: **Christophe Craeye, François Glineur**
Readers: **Eloy de Lera Acedo, Claude Oestges, Jean Cavillot**
Academic year 2018–2019
Master [120] in Electrical Engineering

Université Catholique de Louvain

# *Abstract*

Ecole Polytechnique de Louvain

**Calibration of SKA-low antenna array using drones**

The Square Kilometer Array project goal is to build the next generation of telescope. It will allow us to see the most distant celestial bodies with a resolution and a sensitivity never reached by the current telescopes. The calibration of thousands of the antennas composing the telescope will be necessary to provide these performances. This calibration consisting of finding each antenna radiation pattern using an artificial source mounted on a drone, has already been studied [1] and used in far field for some radio telescopes [2]. In the first part of this Master Thesis, the effect of the impedance of amplifiers connected directly to the antennas will be analyzed. The influence of this parameter on the performances of the calibration using a drone flying in both far-field and near field will also be reviewed. The second part will focus on the calibration of the antennas in the vicinity of a finite ground plane. The effect of this round plane has also been studied and computed [3]. This work will review the possibility of simulating this effect and calibrating the radiation patterns on this finite ground plane using infinite ground plane patterns and the radiation of azimuthal currents on this plane.

# *Acknowledgements*

I would like to thank my advisor Christophe Craeye for his guidance and for his essential reviewing of this Master thesis.
I would like to thank Jean Cavillot for his advices and for the data on the finite ground plane simulations

# Contents

# List of Figures

# Abbreviations

**AUT** **A**ntenna **U**nder **T**est

**FF** **F**ar **F**ield

**FOV** **F**ield **O**f **V**iew

**GNSS** **G**lobal **N**avigation **S**atellite **S**ystem

**GP** **G**round **P**lane

**HARP** **HAR**monic **P**olynomial

**LNA** **L**ow **N**oise **A**mplifier

**MBF** **M**acro **B**asis **F**unction

**MoM** **M**ethod **o**f **M**oments

**NF** **N**ear **F**ield

**PPK** **P**ost **P**rocessing **K**inematic

**RTK** **R**eal **T**ime **K**inematic

**SKALA** **S**quare **K**ilometer **A**rray **L**og-periodic **A**ntenna

**SKA** **S**quare **K**ilometer **A**rray

**UAV** **U**manned **A**erial **V**ehicle

# Chapter 1

# Introduction

Since the Antiquity, mankind has learned a lot by looking at the sky. The knowledge we acquired never stops growing as well as the skills and the tools made to access it. The Square Kilometer Array (SKA) radio telescope project is one of this future tools allowing us to see further and more accurately into the universe.

## 1.1 Radio-telescope

A radiotelescope is made to observe the far-away astronomical objects. However this telescope does not use visible light to produce images but an other part of the electromagnetic waves, the radio-frequency waves. These waves are far lower in the frequency spectrum and can provide other information than the visible light about these celestial objects. They also have the advantage of less scattering through the atmosphere which gives the possibility, compared to visible light, to make survey of the sky during the day without being annoyed by the Sun.

## 1.2 Interferometry

Compared to optical astronomy, radio telescopes are bigger and have a lower resolution namely, the potential for a telescope to distinguish two near points. The resolution is in fact proportional to the radio-telescope size for parabolic/spherical radio telescope. This formula is the origin of the size of gigantic telescope as FAST (figure 1.1) or Arecibo radio telescope. (1.1).

$$\text{Angular resolution}[^\circ] = \ 59.42 \ \frac{\lambda}{D} \tag{1.1}$$

Where D is the actual size of a telescope.
To increase the resolution of radio telescope without building country-size dishes, the solution is to generate a virtually large telescope using many telescopes away from each other. These antennas do not inspect each point of the sky section of interest but a bunch of points at the same time. As these antenna collects slightly different information, they allow one, to reconstruct an image of the celestial body using a specific correlation algorithm. The resolution is no longer

**Figure 1.1:** Five hundred meters Aperture Spherical Telescope in China [4]

the size of the single antenna but the maximum distance between the antennas. This distance can vary: it can be kilometers size like, the VLA (figure 1.2) or way more, like the VLBI [10] for which the antennas used are spread over the world and synchronized using atomic clocks.

**Figure 1.2:** Very Large Array telescope in New Mexico. The array is composed of 28 antenna which can be moved on a three-arms star of 20km each[5]

## 1.3 Square Kilometer Array

The SKA project started in the early 2000's. It consist of an international effort to build the world's largest radio telescope. The SKA is expected to bring us information about:

- Gravitational waves by observing the electromagnetic spectrum radiated by ultra-massive pulsars.
- Dark energy which seems to sometimes counterbalance the gravity force [11].
- The origin of the universe at the Epoch of Reionization [12] when the atoms were ionized by the first generation of stars. This epoch can be studied by looking at the 1420MHz hydrogen line, that has been red shifted [1] below 100MHz.

To do so, the SKA project will focus on the frequency band from 50MHz to 10GHz. As so wide band antenna and electronic system too hard to be build, it is actually composed of many sub radio telescope [6]:

- **High Frequency (from 1500MHz to 10Ghz):** around 3000 parabolic dishes that are more suitable for this frequency band. The steering direction is here set by a mechanical system (figure 1.3).
- **Mid Frequency Aperture Array (from 400MHz to 1500MHz):** The MFAA will take place in a second phase of the SKA deployment. It is based on a high frequency phased array which is there no longer mechanically steerable but uses different phase for each element to point a specific direction. This electronic method allows the system to scan each direction at the same time. The observation time is then significantly reduced compared to a mechanical system.
- **Low Frequency Aperture Array (from 50 to 350MHz):** This part also based on phase array. The array will be decomposed into 512 stations (for the first phased of the project) of 256 log-periodic antennas. Each station contains a local pre-processing unit. They will be located on three spiral arms with a denser central core.

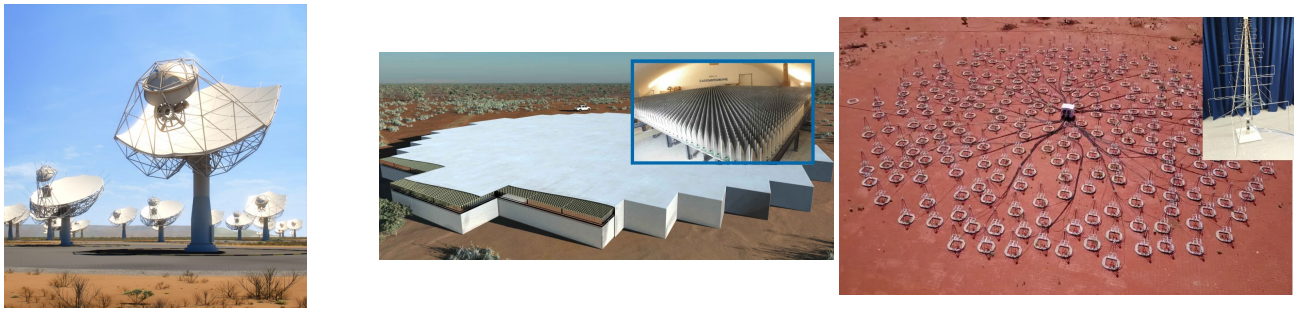

**Figure 1.3:** Antenna arrays from the three part of SKA: a)High frequency 15m dishes [6], b) MFAA array and antenna [6], c) Low frequency (SKALA) and the log-periodic antenna [7]

In this master thesis we will focus on this latter part and more specifically on the antennas in one station.

[1] kind of Doppler effect due to universe expansion

## 1.4 Aim of calibration

The calibration is a key parameter for good measurement. It allows one to verify and adjust systems to fit their expected value with their measured value. Here, with a telescope, we want to know exactly what the antennas are looking at and if they all represent the same power in the same way, we are trying to recover the response of the telescope to the sky. The response of an antenna is represented by the antenna pattern. As the antenna pattern is affected by its surrounding environment, we use the Embedded Element Pattern [13] of the antenna which represents the antenna at its final position in the array accounting for the coupling with other antennas. At the end, each antenna having a different environment, their EEPs are all different. THe aim of this calibration is then to accurately recover these EEPs.

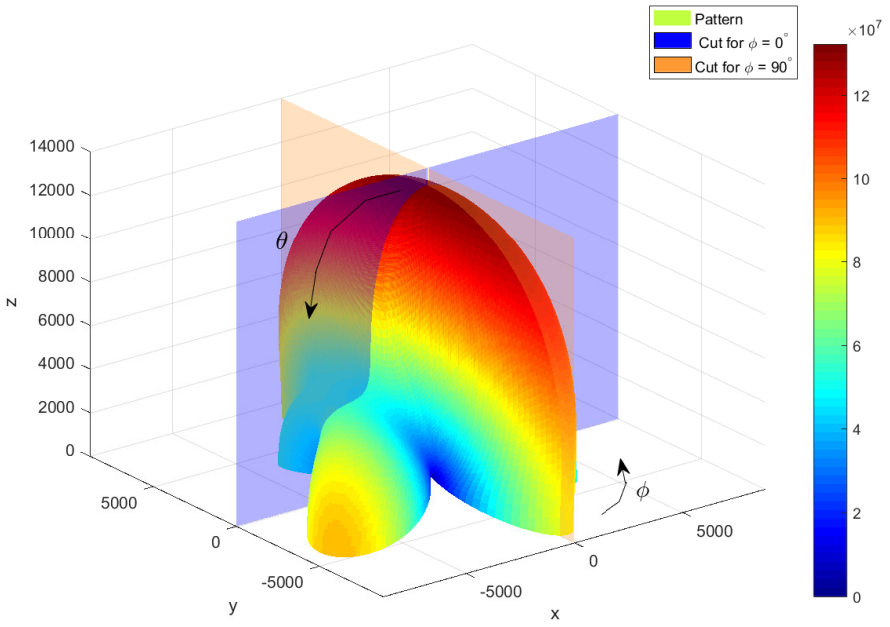


**Figure 1.4:** Cuts made to flatten the 3D antenna pattern to 2D graphs

Once we know accurately the telescope response we can retrieve the incoming signal by de-convolving this transfer function. In the following chapters, only two cuts of EEP and other patterns will be plot to simplify the visualization of the patterns as shown on figure 1.4 .

# Chapter 2

# State of the art

## 2.1 HARP

As said before, the antennas patterns are computed using the HARP software , itself using information specific to mutual coupling, and the Method of Moments (MoM).

### 2.1.1 Method of Moments

The MoM is a well-known numerical method in the antenna field. This numerical technique allows the solution of electromagnetic fields in complex geometries where there is often no analytic solution available. The linear equation mentioned is derived from Maxwell's equations (2.1) [14].

$$\begin{cases} \nabla \times \mathbf{E} = -\dfrac{\partial \mathbf{B}}{\partial t} \\ \nabla \times \mathbf{H} = \mathbf{J} + \dfrac{\partial \mathbf{D}}{\partial t} \\ \nabla \cdot \mathbf{D} = \rho \\ \nabla \cdot \mathbf{B} = 0 \\ \mathbf{B} = \nabla \times \mathbf{A} \end{cases} \iff \begin{cases} \mathbf{E} = -j\omega \left( \mathbf{A} + \dfrac{1}{k^2} \nabla \nabla \cdot \mathbf{A} \right) \\ \mathbf{A}(\mathbf{r}) = \mu \displaystyle\int_{v'} \mathbf{J}(\mathbf{r}') G(\mathbf{r}, \mathbf{r}') dv' \\ G(\mathbf{r}, \mathbf{r}') = \dfrac{e^{-jk|\mathbf{r}-\mathbf{r}'|}}{4\pi |\mathbf{r}-\mathbf{r}'|} \end{cases} \tag{2.1}$$

The linear equation of interest is here linking the electric field $\mathbf{E}$ to the current density $\mathbf{J}$ through the potential vector $\mathbf{A}$ and the Green's function $G(\mathbf{r}, \mathbf{r}')$ for the problem with geometry $\mathcal{G}$

$$\mathbf{E} = \mathcal{L}\left[\mathbf{J}, \mathcal{G}\right] \tag{2.2}$$

The method then consists of segmenting this complex geometry into $N$ sections. For each section, basis functions $\mathbf{f}_n(\mathbf{r}) \ : n = 1...N$ are chosen to be able to generate, through linear combination, the final current density distribution.

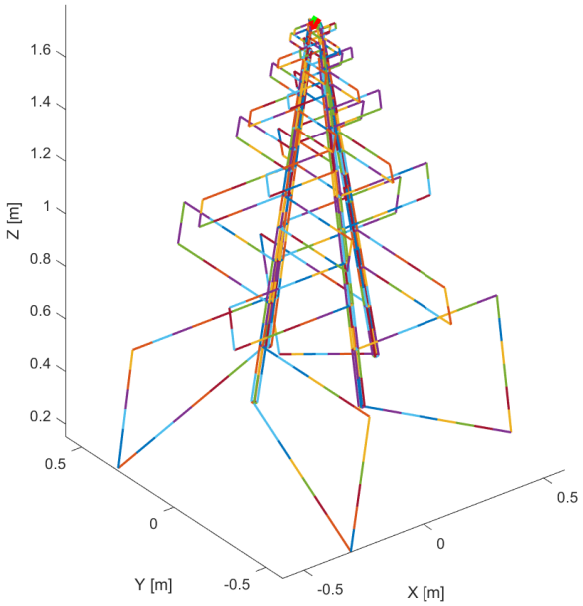


**Figure 2.1:** Mesh of the SKALA antenna and segmentation into basis functions. Feeds are depicted by the red and green (each polarization) on the top.

$$\mathbf{J} \approx \sum_{n=1}^{N} a_n \mathbf{f}_n \qquad \Rightarrow \qquad \mathbf{E} \approx \sum_{n=1}^{N} a_n \mathcal{L}\left[\mathbf{f}_n, \mathcal{G}\right] \tag{2.3}$$

We then define the inner product [1].

$$\langle \mathbf{f}_1, \mathbf{f}_2 \rangle = \int_{\mathcal{G}} \mathbf{f}_1 \cdot \mathbf{f}_2 \tag{2.4}$$

In other to have a residual ( $\mathcal{R} \triangleq \mathbf{E} - \sum_{n=1}^{N} a_n \mathcal{L}\left[\mathbf{f}_n, \mathcal{G}\right]$ ) orthogonal with the solution we need to have

$$\sum_{n=1}^{N} a_n \left\langle \mathcal{L}\left[\mathbf{f}_n, \mathcal{G}\right], \mathbf{f}_m \right\rangle = \langle \mathbf{E}, \mathbf{f}_m \rangle \quad \Rightarrow \quad \mathbf{Za} = \mathbf{b} \tag{2.5}$$

which is a simple linear system of equations easily solvable with standard numerical methods. The $\mathbf{Z}$ matrix linking a form of magnetic field to electric field, it has impedance unit and is called impedance matrix.

### 2.1.2 Macro Basis Function

Once we execute the MoM on the antenna we have the same number of coefficients as the number of sections or basis function. For a complex antenna this number is quite high ( 1218 for SKA-low antennas ) and significantly increases the computational time. These basis functions are then projected on a smaller and more efficient basis. These Macro Basis Functions are then used for the computation of the antenna coupling effect. Their number must increase linearly

[1] also called moment, there comes the designation of the method

with frequency to keep the approximation correct, e.g :15, 20, 45, and 70 at 50, 110, 200, and 350 MHz, respectively [15].

### 2.1.3 HARP

HARP essentially provides the embedded element patterns of all antennas in the array and then enable the array pattern computation. When the MoM is executed and reduced with MBFs, to avoid computing explicitly the interaction between MBFs for each antenna pair, HARP uses an interpolation of the MBF interaction.
First, interaction between a source MBF ($S$) of antenna $n$ set at the origin and a testing MBF ($T$) of antenna m set at different positions: $Z_{TS}^{exact}(r_{mn}, \hat{\alpha})$.
A far-field approximation of the MBF interaction is also computed : $Z_{TS}^{approx}(r_{mn}, \hat{\alpha})$.
Then the difference between these values is used to compute the interpolation harmonic polynomial of the form 2.6.

$$B_{TS}(d(r_{mn}), \hat{\alpha}) = \sum_{p=-P}^{P} e^{jp\alpha} \sum_{q=0}^{Q} c_{pq} d^q = \frac{Z_{TS}^{exact}(r_{mn}, \hat{\alpha}) - Z_{TS}^{approx}(r_{mn}, \hat{\alpha})}{e^{-jkr_{mn}}} \tag{2.6}$$

Where $c_{pq}$ are the coefficients of this interpolation polynomial. This provides a reduced system of equations.
After solution of that system of equations, the interactions between the antennas (divided into MBF) in the array of interest are easily computed by the use of this data [15].

## 2.2 Calibration with a drone

As explained before, the calibration of the radio-telescope is important to produce reliable images at the end of the process. The observed image in eq. 2.7 [16] is represented by the visibility $\widetilde{V}(t)$, the exact image being $V(t)$, the stochastic noise $n_{i,j}(t)$, the possible offset $\epsilon_{i,j}(t)$, and the complex gain of antennas (used for correlation) $g(t)$ which are here the subject of the calibration.

$$\widetilde{V}(t) = g_i(t) g_j^*(t) V(t) + \epsilon_{i,j}(t) + n_{i,j}(t) \tag{2.7}$$

There are different types of calibrations:

- Direct calibration: based on a direct monitoring of critical or a special circuitry feedback parameters that can change and apply a correction. This calibration is not available for all parameters. It is often applied to the electronic circuits following the antenna.

- Self-calibration: based on a prediction of the observed source: max intensity, dimension,... The calibration is made using a close-loop process. From an initial image the system computes corrected coefficients and creates another image. The coefficients are recomputed until the model is reasonably satisfied. This method requires strong signal and specific array properties.

- Calibrator source in the sky: used to calibrate the antenna phase offset. It allows on for instance to determine atmosphere phase shift effect.

- Artificial calibrator: based on the observation of an artificial source, e.g. a source on the top of a tower or, in this case, a drone.

The calibration or pattern measurement of antenna using an Unmanned Aerial Vehicle becomes more and more popular [17].
The procedure consists of having an UAV equiped with 2 antennas , one for each polarization, that hovers over the antenna array at different positions emitting a defined signal, which should normally cover the antenna bandwidth. This signal is then received by each antenna of the array. The set of measurements ($N_a$ antennas times $N_m$ measurements/positions) is then used to compute by comparing measurement and computed fields, coefficients describing each antenna EEP.
In this work, we will use the HARP software to simulate measurements. In this context, we will also through this report, work with the reciprocal problem. This problem works exactly the same way thanks to the Reciprocity theorem of electromagnetics [18] which establishes an interchangeability between the performances of emitting and receiving antennas. Here the property of interest is that the receiving/transmitting patterns are the same.
In this project the antenna EEP are computed using the MBF patterns $\mathbf{p}_{i_m}(\theta,\phi)$ and their coefficients $cf^i_{i_m,i_a}$ found using HARP. The EEP of an antenna in an array of $N_a$ antennas and using $N_m$ MBF is then found .

$$\mathbf{F}^i = \sum_{i_a=1}^{N_a}\sum_{i_m=1}^{N_m} cf^i_{i_m,i_a}\mathbf{p}_{i_m}(\theta,\phi)\; e^{jk(x_a u_x(\theta,\phi)+y_a u_y(\theta,\phi))} \tag{2.8}$$

The indexes $i_m$ and $i_a$ represent respectively the MBF and the antenna. The last factor stands for the phase due to the position of the antenna in the array, $u_x$ and $u_y$ are the components of the unit vector in the direction of observation. The array pattern is then found by summing up the antenna EEPs weighted by their input current.

The technique has been studied before for the SKALA [1]. This consists of collecting data on the antenna pattern through $N_e$ *experiments* and of using it to correct the deviations of the real EEP compared to the EEP computed. The correction is introduced by using complex coefficients $c^i_{i_a}$ on each antenna $i_a$ contributing to each EEP $i$ which gives a total of $N_a^2$ coefficients for the whole array. Finding these coefficients requires solving a set of $N_a$ systems of $N_e$ equations with $N_a$ unknowns[2].

$$\overline{\mathbf{F}^i_v} = \underbrace{\sum_{i_a=1}^{N_a}\sum_{i_m=1}^{N_m} cf^i_{i_m,i_a}\mathbf{p}_{i_m}(\theta,\phi)\; e^{jk(x_a u_x(\theta,\phi)+y_a u_y(\theta,\phi))}}_{\mathbf{B}^i_{v,i_a}}\; c^i_{i_a} \tag{2.9}$$

Minimizing the error between calibrated and computed pattern now reduces to a solution in the

[2]The vectorial notation for $\overline{\mathbf{F}^i_v}$ is here used for representing each experiment and no more for the physical vector

least-squares sense.

**Near Field** : The problem before was found considering that we directly measure the pattern of the antenna. Nevertheless the UAV does not capture it directly but records a voltage through its antennas. On the other hand the calibration described before requires flying beyond the Fraunhofer distance which is inversely proportional to the wavelength and depends on the array size $D$ and reaches a maximum value for the SKALA station of about 3 km.

$$r_{_{UAV}} \gg \frac{2D^2}{\lambda} = R_{Fraunhofer} \quad r_{_{UAV}} \gg \lambda \quad r_{_{UAV}} \gg D \tag{2.10}$$

This constraint may completely discard the use of the drone due to battery autonomy or the current legislation for UAV. This can be solve through the array near-field calibration. This approach consists of having the drone flying in the array near-field but still in the antenna far-field[3] to keep the definition of antenna patterns correct. The method is similar to far field calibration but as the UAV flies closer to the array, each antenna pattern must be evaluate at different elevation and azimuth due to drone relative position. The voltage measured by the drone on its $k^{th}$ antenna having the pattern $\mathbf{F}_k^d(\hat{u}_{i_a}, \Omega)$ in the direction $-\hat{u}_{i_a}$ a unit vector form the antenna pointing to the drone.

$$V_k^\tau = \sum_{i=1}^{N_a} \frac{2\lambda Z_L}{j\eta} \sum_{i_m=1}^{N_m} \sum_{i_a=1}^{N_a} \mathbf{F}_k^d(-\hat{u}_{i_a}) \cdot \mathbf{p}_{i_m}(\hat{u}_{i_a})\ cf_{i_m,i_a}^i\ V_i^t \underbrace{\frac{e^{-jkR_{i_a}}}{R_{i_a}}}_{\text{Propagation for near field}} \tag{2.11}$$

## 2.3 Types of non idealities

There are two different kinds of non idealities: the ones intrinsic to the antenna and the whole system, and those linked to the calibration.

### 2.3.1 System non idealities:

**Amplifier transfer function:** The complex gain of these amplifiers is defined by their transfer function for all frequencies but as any electronic component, it exhibits some variations. These variations can come from the fabrication process which can not produce exactly identical amplifiers, from power supply or from the temperature. This one can be very important because of the location of the SKALA in the Australian desert, with temperatures from 0°C to 48°C in the the shade [19]. As this parameter is simply a complex factor it can easily be corrected through the calibration.

[3]We can settle for the array NF because the antenna NF limit is low enough, ≈ 6 m

**Amplifier input impedance:** This parameter only depends on the first amplifier, the LNA, input impedance contrary to the previous one. Since this amplifier is directly connected to the antenna, this impedance affects the antenna pattern. This effect will be studied in Chapter 3 of this report.

**Antenna pattern:** The antenna pattern may differ from the simulated one. That may come from many parameters from the antenna geometry or from the environment around it. This non-ideality is more complex to handle since, by definition, it is direction dependent

### 2.3.2 Calibration non idealities:

**Drone system:** Just as the antenna array, the drone used for calibration needs to have a known directivity and emitted power. These are also affected by drone amplifiers and antennas.

**Drone position and attitude:** To correctly analyze the pattern the measurement positions must be known accurately. The effect of these imprecision effects has been studied in [1]. The positions considered with a standard deviation of 0.1m in near field calibration still generates good results. The GPS base accuracy being 10m it must be increased by some side hardware. The use of the GPS carrier frequency phase is one of the key points of accuracy increasing techniques. In Real Time Kinematic (RTK) a base station at a well-known location computes the phase of the carrier and make estimation on ionospheric and tropospheric delay to send a correction signal to the estimation done by the UAV (figure 2.2) [20]. Like Differential GNSS, the position accuracy achievable by the drone depends on, among other things, its distance from the base station and the accuracy of the differential corrections. This technique can reduce the error to 2cm in the horizontal plane and 8cm for the altitude.
For the problem of calibration the use of a precise real time positioning algorithm is not compulsory: as long as the measurement position are not far from the wanted path, the exact positions can be extracted, just before the calibration coefficient computation since we just want an a posteriori knowledge on it. We can also use the array it-self to estimate the drone position is also possible but is much more ambitious. An variant of the RTK system is the Post Processing Kinematic (PPK) system which works exactly the same but correction are made in a post processing step.
The attitude must also be monitored to correctly find the drone antenna orientation with respect to the array.

## 2.4 Ground effect computation

In the original HARP software, the ground effect is simulated using the images method consisting of considering the ground as an infinite Perfect Electric Conductor acting like a mirror. A

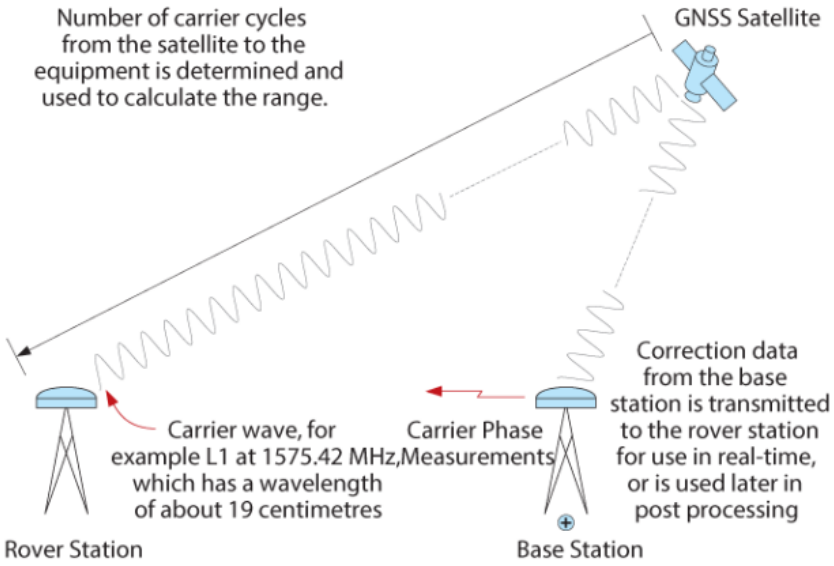


**Figure 2.2:** Schematic of the RTK system [8]

virtual antenna is then located symmetrically from real antenna with respect to the ground to ensure a null electric field on the ground plane. The pattern is then computed summing up the contributions of virtual and real antennas.

The hypotheses underlying this method are unfortunately too strong by deviating from the real ground conditions: the real metallic ground plane is not infinite and outside this quasi-PEC ground plane, the soil is neither PEC nor air, i.e. it has non-zero electric permittivity and conductivity.

The method chosen here [3] to simulate the ground plane effect, consists first of computing the electric incoming field for the finite ground plane. This step is carried out using a spectral approach to reduce the computation complexity. In a second step the MoM is applied to compute the induced currents. The incident fields, from the antennas onto the ground plane are computed with the help of a Green's function that accounts for a layered-medium as a soil. The currents on the antennas themselves are assumed identical to those in presence of an infinite ground plane.

# Chapter 3

# Load impedance effect on calibration

In this chapter, we will first discuss about the origin of the load impedance variation. Then we will compute the EEPs using different loads to analyze the effect of the impedance of the load of the antenna on the EEP of this antenna and its close neighbors. At the end, we will try to see if the calibration presented in [1] can manage to correct the impedance effect without knowing their effective value.

## 3.1 Impedance variation

This section will review the three main origins of the impedance variability. A fourth one could be added, the state of the LNA (operational or broken). This parameter can be easily determined and located as soon as extreme impedance values are obtained. Then the antenna can often be considered as open circuit or the LNA board can be swapped with a new one.

**Frequency**

The antenna and the amplifier are both wide-band systems. A precise design on the whole bandwidth for these kinds of devices is generally hard to achieve. Then the system must deal with the variation according to frequency of its parameters such as gain or input impedance. We can see on figure 3.1, the measured impedance of antenna and LNA.

**Process variation**

This factor is simply due to the imperfection in the fabrication of LNA board and components.

**Temperature**

The temperature of the electronic component may also change the characteristics of the amplifier. The transistors of the amplifier are the most sensitive components of the LNA because they may see their threshold voltage and trans-conductance gain change a lot with temperature. As

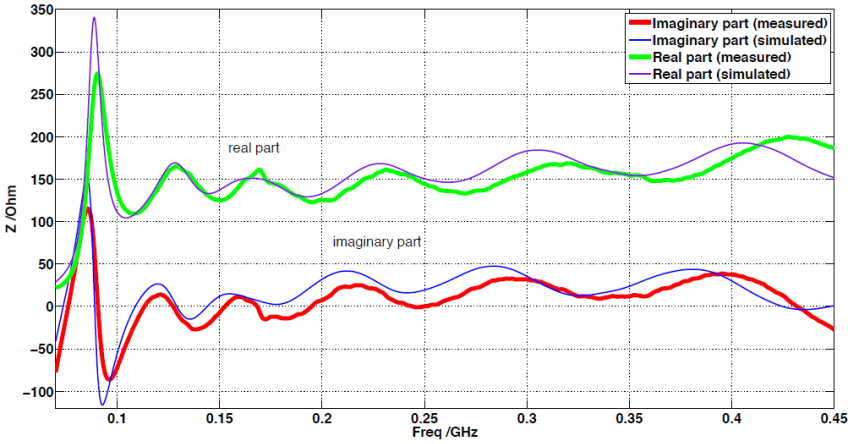


**Figure 3.1:** [7]: Impedance of the SKALA antenna and LNA.

discussed in the Section 2.3.1, the weather condition in the desert makes this temperature vary a lot during the year, maybe leading to the need for more frequent re-calibrations.

## 3.2 Computation of the pattern using different loads

### 3.2.1 Open circuit, short circuit and embedded element pattern

One way to change the load impedances of an antenna array without recomputing the whole antenna MoM and coupling matrix is to go through the open-circuit pattern [13], or the short circuit pattern.

The field radiated at a distance $R$ by one antenna $i$ feed with an equivalent Thevenin voltage source of $V_i^g$ in an array where the other antennas are not supplied $V_{j\neq i}^g = 0$ (figure 3.2), is given by equation (3.1). There comes the definition of the embedded element pattern $\mathbf{F}_{i,v}^e$ a vector dependant on observation direction direction.

$$\mathbf{E_{i,v}}(R) = \mathbf{F}_{i,v}^e \frac{e^{-jkR}}{R} V_i^g \tag{3.1}$$

One may also determine the field radiated by an antenna with current $I_i$ while other antennas are open-circuited $I_{j\neq i} = 0$ (figure 3.2 ). This defines the open-circuit pattern $F_{i,v}^{oc}$. The open-circuit pattern is often considered very close to the isolated element pattern, but that analogy is only exact for single-mode or minimum scattering antennas [13].

$$\mathbf{E_{i,v}}(R) = \mathbf{F}_{i,v}^{oc} \frac{e^{-jkR}}{R} I_i \tag{3.2}$$

A third type of pattern is the short circuit pattern [21] which works the same as the EEP except that the other antennas are now short-circuited $Z_{Lj\neq i} = 0$ (figure 3.2 $c$).

Using the Thevenin representation of the generator and the coupling matrix $\mathbf{Z}$ it is possible to link current on antenna $i$ to the equivalent generator source. We can also link the EEP to the open circuit pattern :

$$\mathbf{F}_v^{oc} = (\mathbf{Z} + \mathbf{Z_L})\mathbf{F}_v^e \tag{3.3}$$

Where $\mathbf{F}_v^{oc}$ and $\mathbf{F}_v^e$ are now matrix with as many lines as there are antennas in the array, and one column per direction inspected. This relation being correct for different sets of loads and their EEPs, we can easily know the EEPs for the loads used or envisaged from the EEPs from a already known for a given set of loads

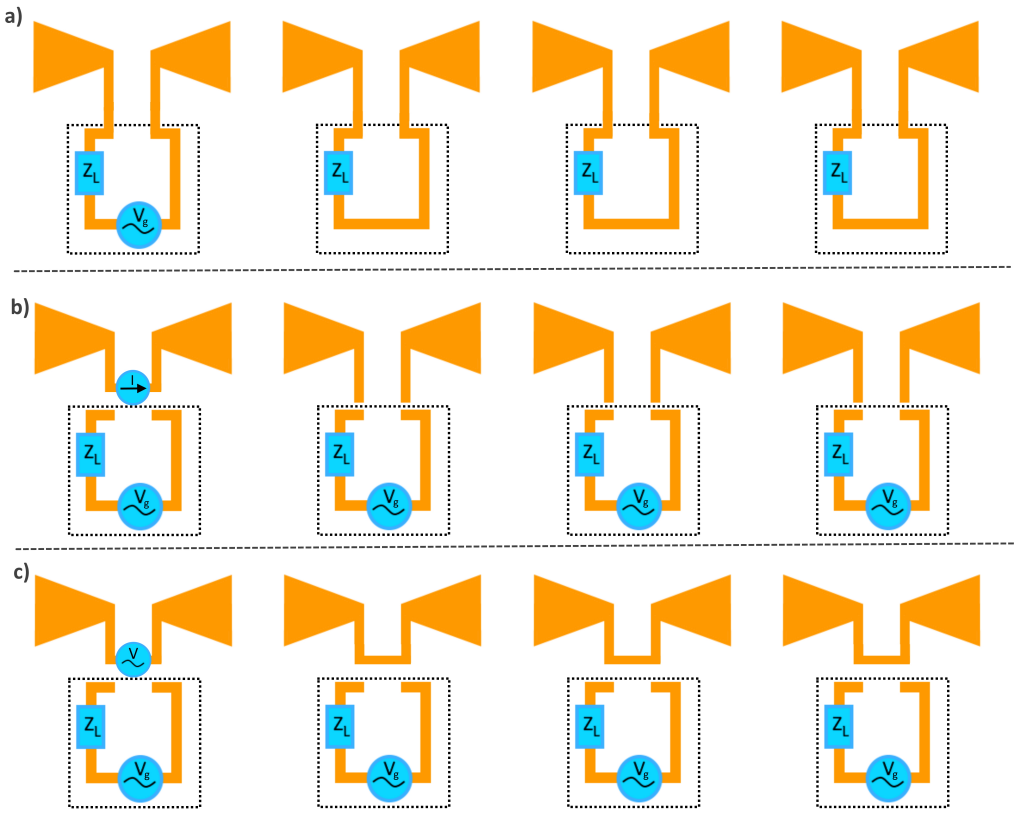


**Figure 3.2:** *a*) Embedded element pattern configuration, *b*) Open circuit pattern configuration, *c*) Short circuit pattern configuration

### 3.2.2 Near field

Unfortunately, relation (3.3) is only available in far-field conditions. The coupling matrix must then be recomputed for a new set of impedances, which does not take too much time, given the HARP software [15] efficiency. To avoid the full re-computation of the MoM matrix for each different load, the value of the impedance is changed during the MBF coupling matrix

computation:

$$\mathbf{Z}^r_{self} = \mathbf{Q}^H \mathbf{Z}_{self} \mathbf{Q} \quad \rightarrow \quad \mathbf{Z}^r_{self,i} = \mathbf{Q}^H \mathbf{Z}_{self} \mathbf{Q} - Z_{L,i} \mathbf{q_s}^H \mathbf{q_s} + Z_{L_0} \mathbf{q_s}^H \mathbf{q_s} \tag{3.4}$$

Where the $(^H)$ superscripts stands for transpose-conjugate.

The operation consists of changing the basis function self-impedance matrix entry corresponding to the antenna inputs (one input for each polarization). The column of the transformation matrix $\mathbf{Q}$ from basis function to MBF corresponding to the updated input is extracted to introduce directly the impedance change.

### 3.2.3 Effect of the load on EEP

We can then plot the patterns for different antenna loads. On figure 3.3, the EEPs are plotted for an array of two antennas spaced two meters apart for extreme load cases. We see that on antenna 1 with the normal, short circuited and nearly open loads, the EEP is strongly affected by the impedance matching: the directivity is quite the same but the power radiated change as expected. This case should easily be solved with a calibration using only one coefficient by antenna. Moreover, knowing the antenna impedance and the source power, we can readily recover the load impedance used from the pattern.

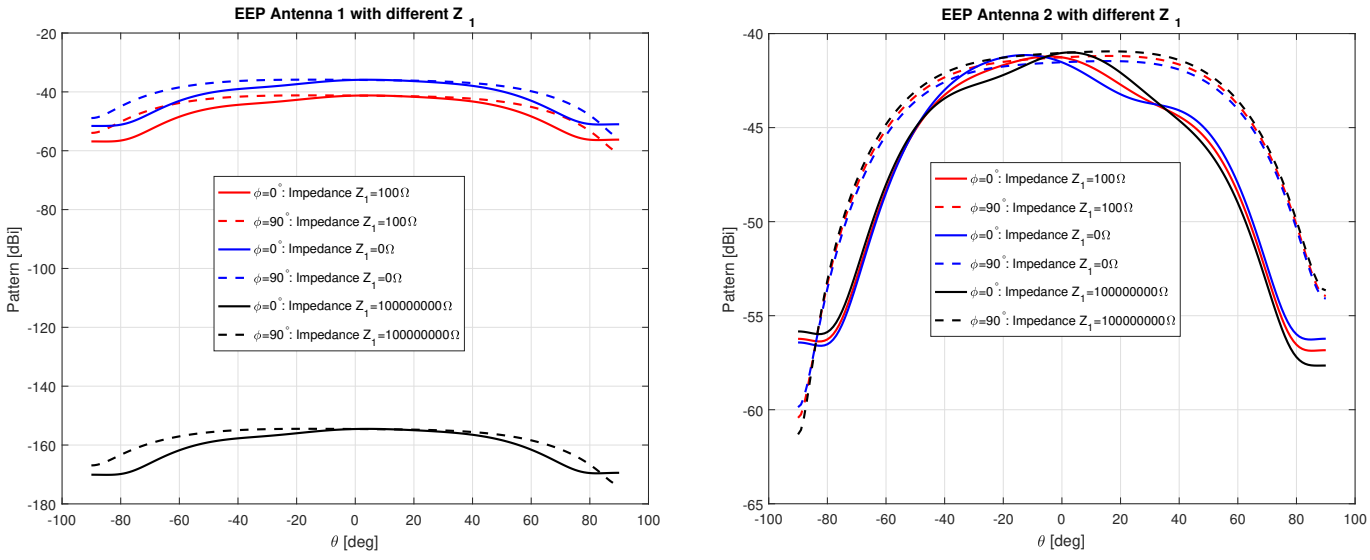


**Figure 3.3:** Antenna EEP at 110MHz for the first and the second antenna with open, short, and normal load for antenna 1 and a 100Ω load on antenna 2.

For the second one the effect is more complex. The load impedance of this antenna is matched but due to mutual coupling, the pattern is affected by the radiation of the current generated by the second antenna on the first one.

To quantify the variation of the EEPs from the EEPs computed with a standard 100Ω amplifier input impedance, we will keep the error definition used in [1]:

$$e_{\phi,\theta} = 10\ \log_{10}\left(\left|\mathbf{E}_v - \overline{\mathbf{E}}_v\right|^2 + \left|\mathbf{E}_h - \overline{\mathbf{E}}_h\right|^2\right) - 10\log_{10}\left(\max_{\phi,\theta}\lim_{r\to\infty}|\mathbf{E}(r,\theta,\phi)|^2\right) \tag{3.5}$$

The scalar quantities resulting from it, the maximum (3.6) and mean error (3.7), will also be used to compare the effects of different parameters

$$e_M = \max_{\phi,\theta}(e_{\phi,\theta}) \tag{3.6}$$

$$\mu_e = \mathbb{E}(e_{\phi,\theta}) \tag{3.7}$$

### Distance

The first phenomenon which determines the effect of the loads on the EEPs is the mutual coupling between antennas. This parameter is a direct consequence of the proximity of antennas. As we can see on figure 3.4, the pattern changes shape for different distances between two antennas.

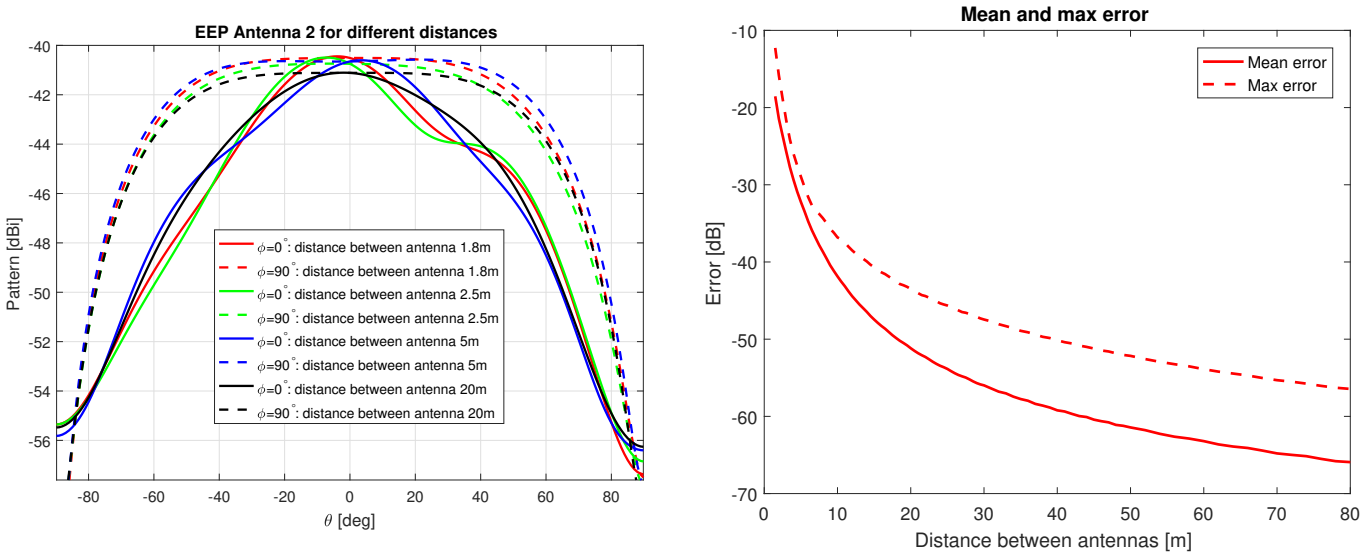


**Figure 3.4:** EEP of antenna 2 in a array of two antenna with different distances (left). Effect of coupling on the mean and max error for many distance with respect to the isolated pattern (right). Both graphs for a 100Ω load.

This effect is indeed less present for widely spaced antenna arrays and the pattern tend toward the isolated antenna pattern (≈ black curve). We can see the exponential [1] decrease of the error between isolated antenna and the embedded element pattern.

[1] linear in non-dB scale

**Frequency**

The pattern of course also changes with the frequency. Intuitively for frequencies producing a lower radiation in the horizontal plane, there may be less influence on other antennas. But we have to remember that the pattern definition is limited to the far field of the antenna. In the near field, intricate interactions between antennas may take place generating coupling between the two elements.

**Impedance**

The effect has already been discussed before, while looking at the extreme cases of open and short-circuited patterns. Changing the impedance of an antenna changes its radiated power due to a voltage divider bridge made by the generator and the antenna impedance, but the directivity keeps quite the same. Instead of this, the EEP of an antenna near the one with a modified load, will see its directivity change while keeping roughly the same radiated power (figure 3.5).

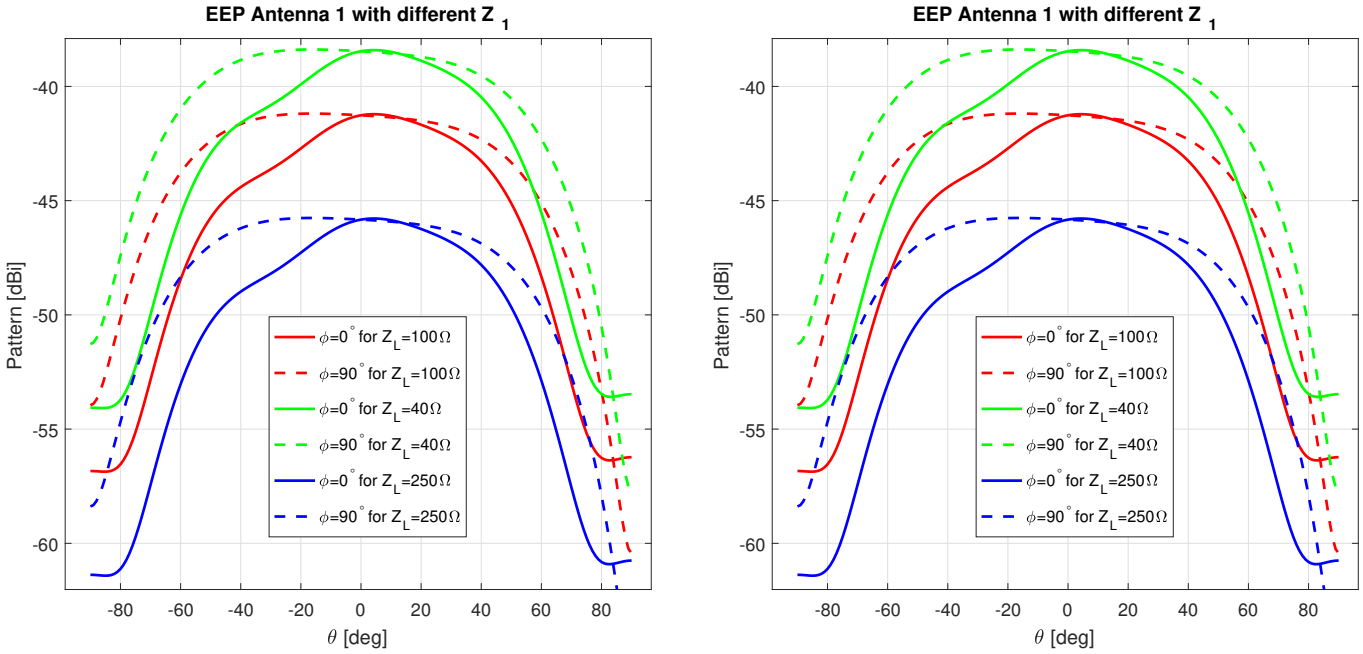


**Figure 3.5:** EEP at 110MHz of antenna 1 (left) and antenna 2 (right). Antennas are 2m apart with different loads for the antenna 1.

For different loads variation (figure 3.6), the error increases in a logarithmic way relatively to the original impedance for both real and imaginary parts. We can also notice that the error evolves the same way for the antenna with the changed load and its neighbor.

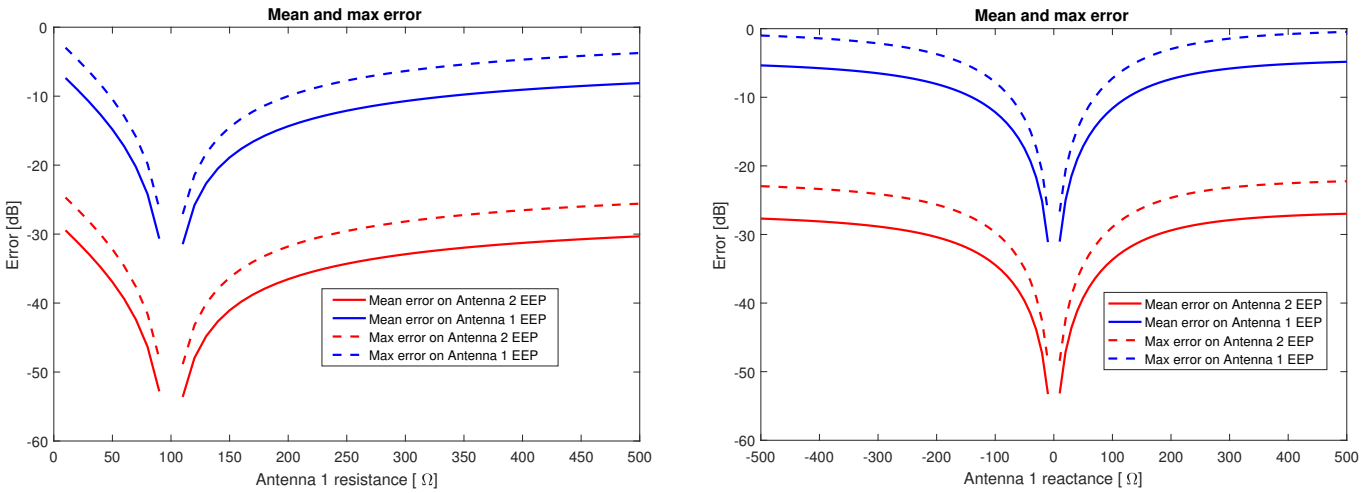


**Figure 3.6:** Maximum and mean error on antenna EEP for different values of the load resistance (left) and of the load reactance (right).

## 3.3 Far-field calibration

We will first investigate the calibration based on measurement far away from the array. Although this approach is difficult to put in practice with a drone, it gives a good introduction to the calibration and to provides insight on the feasibility of the calibration using $N_a$ coefficients for each EEP while having an unknown variability of load impedances.

### 3.3.1 Drone Path

The UAV path influence on calibration has been already studied in [1]. The best choice was to have a quite uniform distribution of measurement points. The solution chosen here is to have a drone following a Archimedean spiral with a nearly equi-spaced measurement points (figure 3.7). The path must also be short given the limited battery autonomy of the drone. The spiral is one of the paths that smoothly travel among all the points while still having a minimal length. Since we are looking for far field conditions in this section, the drone path is necessarily quite long. To reach measurement points up to $\theta = 60°$, the path length is around 53 500 m long.

### 3.3.2 Calibration and results

The calibration goal consists of finding for each antenna EEPs, the weighting coefficients to apply to all EEP. These weighting coefficients are found comparing the measured pattern with the weighted sum of the pattern (2.9). The total number of coefficients to be determined is $N_a \times N_a$. Each of the $N_e$ experiments leads to $N_a$ received signal on antennas. We should then be able to solve this system of equations by mean of least square, by having at least $N_a$ independent experiments.

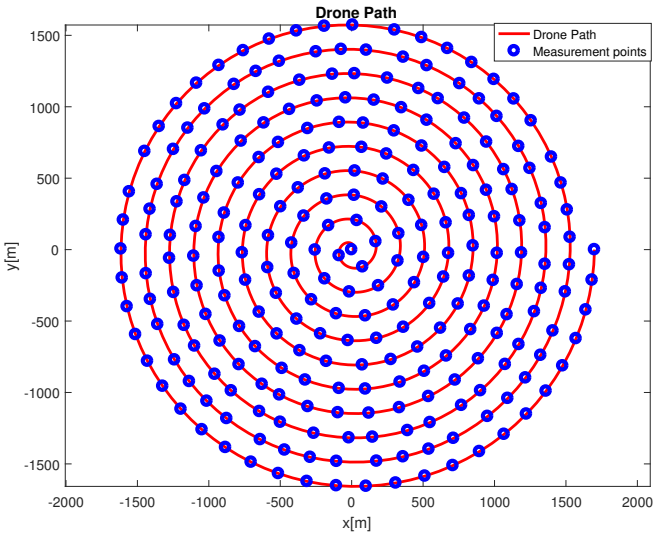


**Figure 3.7:** Drone path and measurement points.

The synthic measurements, here, correspond to the far field EEP of antennas accounting their load is not exactly 100 Ω, load but an impedance randomly chosen between 50 to 150 Ω. On the other side, the EEP used to calibrate the array are computed from a uniform 100 Ω load impedance array. The goal here is to find if this lack of precise knowledge about impedance may corrupt the calibration procedure.

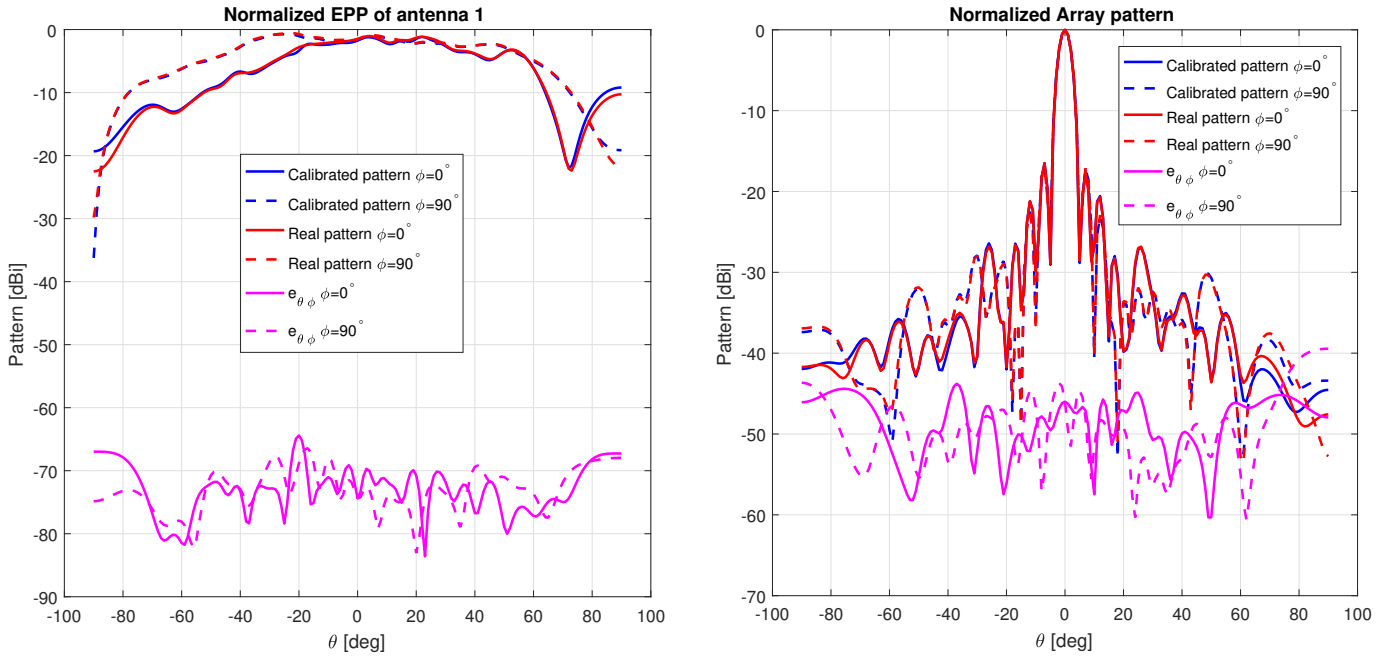


**Figure 3.8:** Calibration result in far-field on EEP antenna 1 (left) and on array pattern (right) at 110MHz with $N_a = 256$ antennas and measurements

On the figure 4.10, we can see that even with unknown loads, the calibration corrects nicely

the EEP with a mean error of $-72$ dB. The patterns start to diverge after $\approx 60°$ due to the lack of measurements in these directions. We can observe the same behaviour on the normalized array pattern.

## 3.4 Near-field calibration

The calibration in far field have many disadvantages due to the altitude of the drone:

- UAV legal altitude limit quite low even if drone can reach altitudes up to 3km.
- Drone path length: already 53 km for the mid-frequency to reach $\theta = 60°$.
- Duration of the calibration: the drone having to go higher and further, duration increases.

The near-field calibration is then a good alternative even if it has a higher computational complexity. The patterns from individual antennas can no longer be added directly since an antenna does not see the drone at the same relative positions as other antennas. The pattern values must then be evaluated at the $N_e$ experiments positions for each of the $N_a$ antennas.

### 3.4.1 Drone Path

Since the drone is flying in the near-field region, the spiral followed by the drone can be shrunk. The same maximum distance from the center as the one used in [1] is use to generate the path. The total path length for a 256 measurements calibration is about 1100 meters. For a calibration using 1024 measurement points, the spiral is wounded up more finely to keep a near equi-spaced points distribution. The path is then longer, around 1890 meter. These lengths are far more reasonable with regards to the UAV autonomy. Near field also means a lower altitude. Now the drone hovers at 10 m above the ground.

### 3.4.2 Calibration and results

For the near field calibration, a more precise model for the measurement and estimated EEP is used. In this section, we are no longer comparing the EEP measured to the EEP computed. Instead, the voltage received by the drone antennas is used (eq. 2.11). It allows us to account for the non-isotropic antenna of the drone and the pitch, roll and yaw angles describing the drone attitude (figure 3.10).
A first simulation concerns the same 256-antenna array as for the far-field case shown on figure 3.11, with $N_a$ experiments with no uncertainty on positions and attitude of the drone.
We can see that the error is correctly reduced by the calibration and reach approximately the same values obtained with the far field calibration and even better for the side lobes given that the drone can more easily reach these angles.

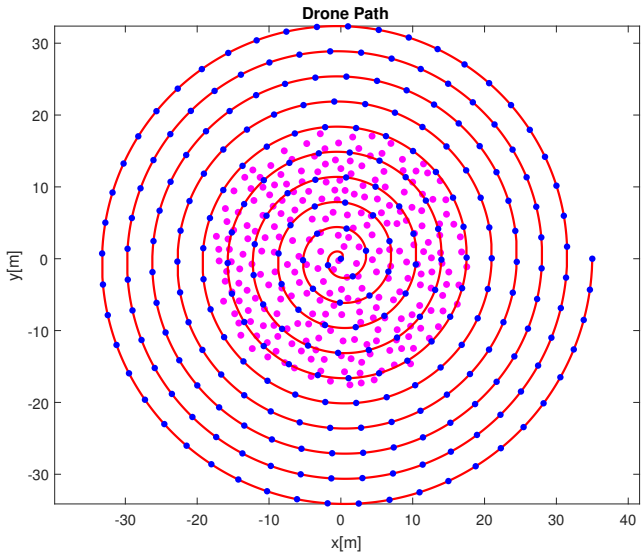


**Figure 3.9:** Drone path (red), measurement positions (blue) and antenna positions (magenta) for NF calibration.

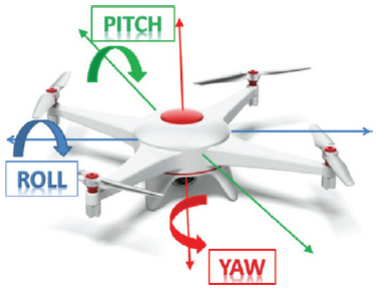


**Figure 3.10:** [9] Attitude angles of a drone

Figure 3.12 represents the calibration when noise is added on the position of the drone and attitude but having more measurements points (1024). The error on the position used is the standard error value for RTK (see section 2.3.2): 2 cm standard deviation in the horizontal plane, 8cm for the altitude and 4 degrees for the attitude angles.
As expected, the error on the EEP increases. The error precedently modest on the side lobes comes back to the mean which, as we can imagine comes, from the larger error on the altitude that has a more significant effect on the measurements on the side of the pattern.

## 3.5 Conclusion

The goal of this chapter was to determine the feasibility of the calibration of an antenna array with inexact load impedance using $N_a$ coefficients per EEP. The concept has also been tested under noisy measurement positions. Table 3.1 shows the errors according to the different calibration methods and conditions. The error is not significant regarding to the calibrated patterns. Indeed, the most important effect being the voltage divider, he is completely balanced

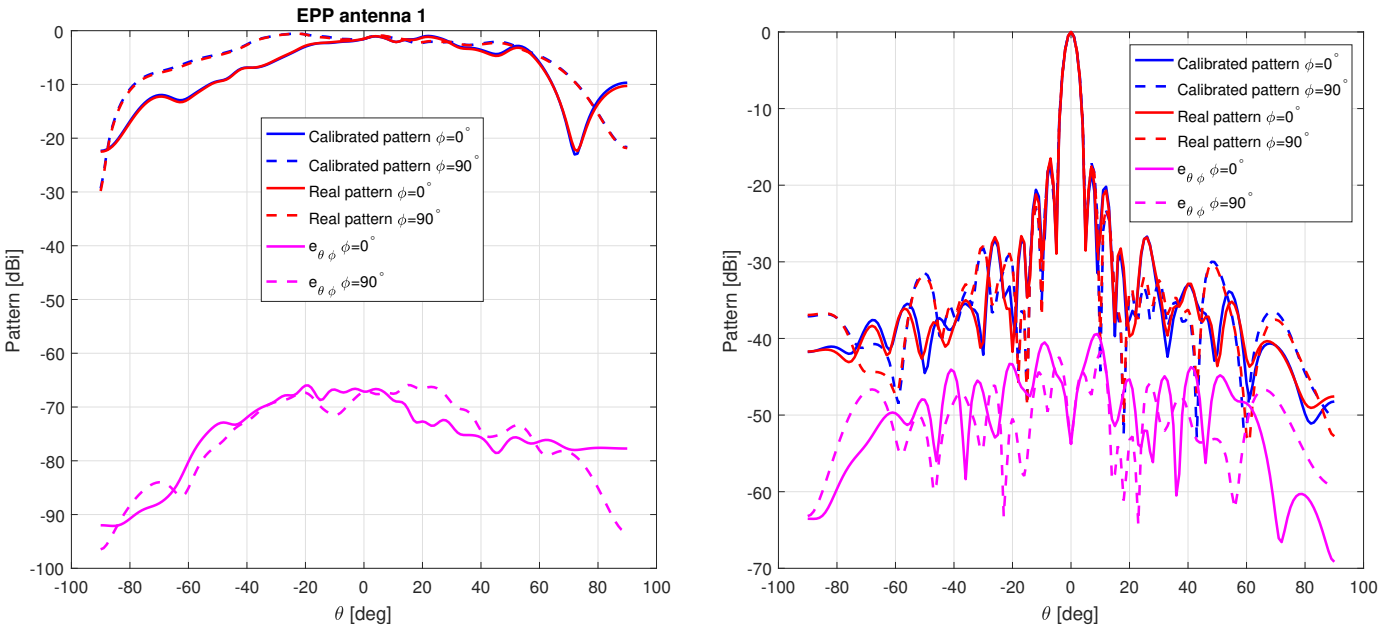


**Figure 3.11:** Calibration results on EEP antenna 1 (left) and on array pattern (right) for a frequency of 110MHz

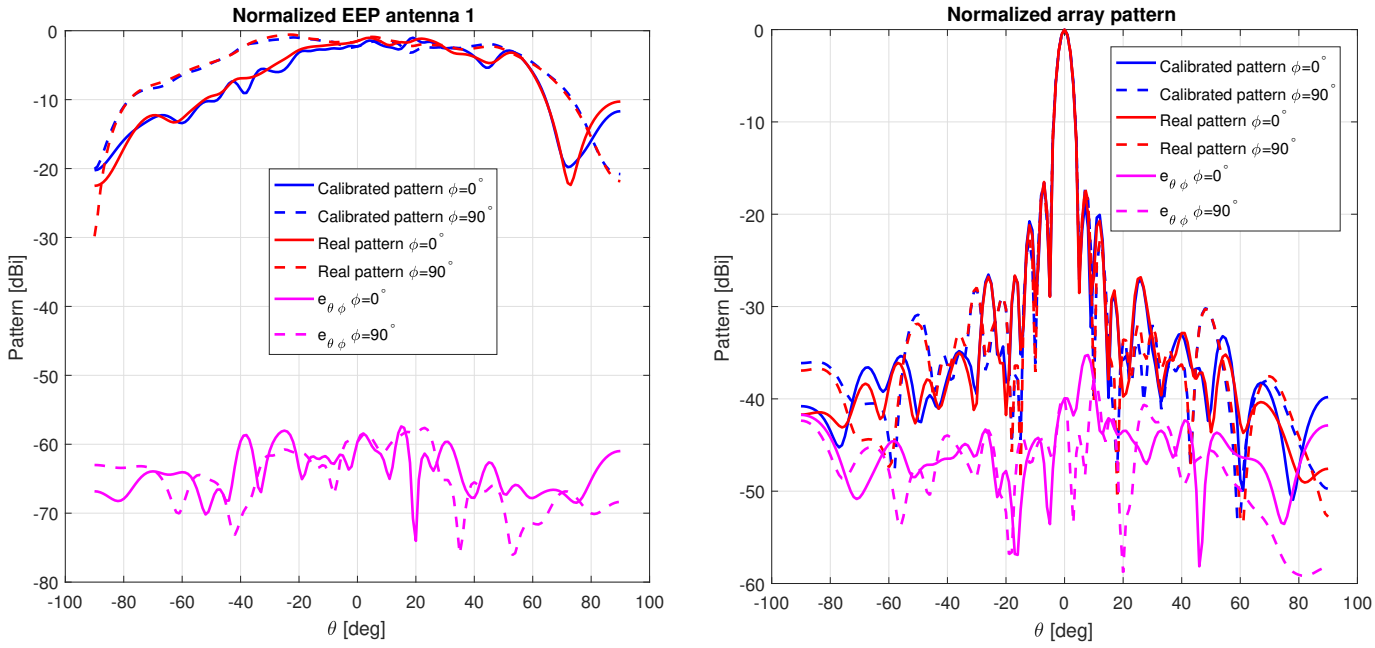


**Figure 3.12:** Calibration results on EEP antenna 1 (left) and on array pattern (right) with noise on position and attitude and 1024 measurement points for a frequency of 110MHz.

by the calibration consisting of multiplying the whole pattern by a constant factor. The other effect changing the shape of the neighbor antenna may also be partially accounted for by the model given the degrees of freedom on the non-excited elements contribution.

| | $\mu_e$ [dB] | $e_M$ Error [dB] | $\mu_e$ on AP [dB] | $e_M$ on AP [dB] |
|---|---|---|---|---|
| Ideal Far Field $N_e = N_a$ | -72.5 | -61.3 | -49.6 | -37.49 |
| Ideal Near Field $N_e = N_a$ | -73.6 | -64.5 | -50.3 | -37.7 |
| Noisy Positions<br>Near Field $N_e = 4N_a$ | -64.0 | -52.0 | -45.8 | -34.8 |

**Table 3.1:** Summary of the different max and mean values for the error for the studied calibrations with loads varying between 50 and 150 Ω

# Chapter 4

# Finite Ground plane computation

Section 2.4 has briefly described the method used to compute the EEP of the antenna in the vicinity of a finite ground plane [3]. The method presented in this section suggests to replace the full computation of the finite ground plane field by the calibration of azimuthal currents on this ground plane and the infinite ground plane pattern of the antenna. The first part will consist of determining the minimal set of coefficients to represent the actual EEP of a given element. The calibration procedure will consist of deriving those coefficients from measurements.

## 4.1 Method

Up to now, the embedded element pattern was computed using an infinite ground plane due to the low computational complexity using method of images. The main idea of the method is to use a distribution of point sources on the ground plane to fill in the difference between the pattern on finite $\mathbf{F}^{fin}$ and infinite $\mathbf{F}^{inf}$ ground planes.
By going from infinite to finite GP, we roughly suppress the induced current outside the finite metallic plane and as we add a new boundary, the current close to it should be slightly modified as well. The current at the center of this plate should normally remain very similar since it do not see the boundary. The suppressed currents outside the plane are in principle lower due to the distance from the radiating antenna but we still want to deal with their effect on the pattern. These are the two main reasons for simulating the GP effect using azimuthal current on the boundary of the circular GP.

Figure 4.1 shows how the currents will be arranged on the finite plane (in red) and the currents implicitly present, computed with the method of images on the infinite ground plane ( light blue).

$$\min_{\alpha_{i_c}} \left| \underbrace{\left( \mathbf{F}^{inf}(\hat{\mathbf{u}}) \; + \; \sum_{i_c=1}^{N_c} \alpha_{i_c} \mathbf{G}_{i_c}(\hat{\mathbf{u}}) \right)}_{\overline{\mathbf{F}^{fin}(\hat{\mathbf{u}})}} - \mathbf{F}^{fin}(\hat{\mathbf{u}}) \right|^2 \tag{4.1}$$

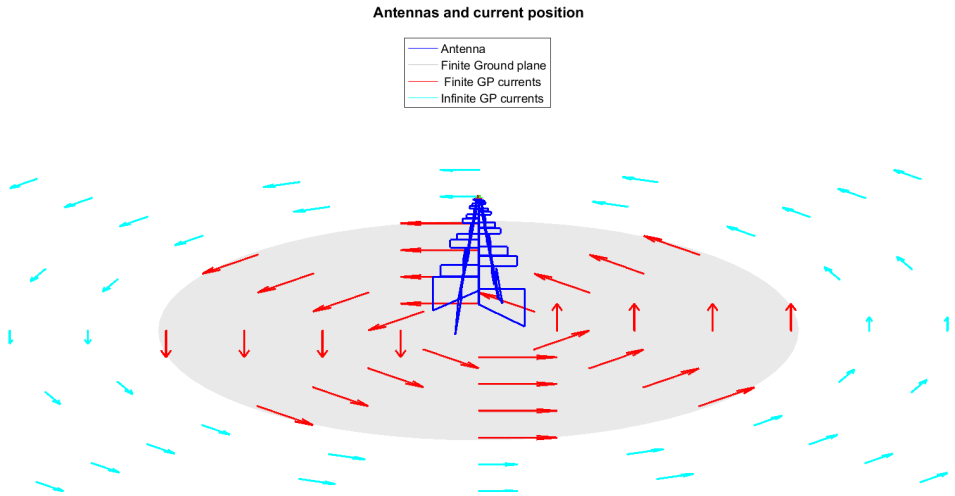


**Figure 4.1:** 3D view of the type of current distribution used to simulate the finite ground plane

The problem is in the form of a minimization of the error between the estimated finite GP pattern $\overline{\mathbf{F}^{fin}}(\hat{\mathbf{u}})$ and the actual finite GP pattern (eq. 4.1). The solution of this least square problem will give us the coefficients or intensity of the currents $\alpha_{i_c}$ to apply on each azimuthal point source pattern $\mathbf{G}_{i_c}(\hat{\mathbf{u}})$.

### 4.1.1 Punctual azimuthal pattern computation

The aim here is not to compute the current distribution exactly but to replace it by point sources on the ground plane surface using the equivalence principle. This principle says that the radiation of any source can be represented by replacing the medium of source it contains by equivalent magnetic and electric sources on the surface.

We can easily find the radiated field of a point source using the general formula for antennas 4.2.

$$\mathbf{E}(\hat{\mathbf{u}}, R) = \frac{-j\eta}{2\lambda} \int\int\int_V \frac{e^{j\ k\ R}}{R} (\mathbf{J}(x,y,z) - \hat{\mathbf{u}}\ (\mathbf{J}(x,y,z) \cdot \hat{\mathbf{u}}))dV \tag{4.2}$$

Where we can find the impedance of free space $\eta$, the wavelength $\lambda$, the wavenumber $k$, the unit direction of propagation vector $\hat{\mathbf{u}}$, the source current $\mathbf{J}$ at position $(x, y, z)$, the distance between the source and the calculated field $\mathbf{E}$
Computing the pattern and the Dirac-delta form of the current largely simplifies the formula to equation 4.3 where $\mathbf{x}_c$ is the distance of the current to the centre of the array.

$$\mathbf{G}^{e}_{i_c}(\hat{\mathbf{u}}) = \frac{-j\eta}{2\lambda}(\mathbf{J}(x,y,z) - \hat{\mathbf{u}}\ (\mathbf{J}(x,y,z)\cdot\hat{\mathbf{u}}))\ e^{j\ k\ \mathbf{x}_c\cdot\hat{\mathbf{u}}} \tag{4.3}$$

We also need the electric field radiated by magnetic current. This current is composed of fictitious moving magnetic monopoles. It helps to extend the symmetry between magnetic and electric fields. The expression of the magnetic field **H** generated by a magnetic current is the same as the expression of the formula for an electric field generated by an electric current. When we have this **H** field we need to re-transform it to electric field using the relation for electromagnetic wave 4.4.

$$\mathbf{E}(\hat{\mathbf{u}}) = \eta\ \mathbf{H}(\hat{\mathbf{u}}) \times \hat{\mathbf{u}} \tag{4.4}$$

This magnetic current has the advantage of generating an electric field with a polarization orthogonal to the electric field of the electric current pointing in the same direction.

## 4.2 Estimation of the finite ground plane effect using current

In this section, we will review the possibility and number of degrees of freedom needed to fit the pattern obtained 8m- diameter circular ground plane with soil (figure 4.2). Two different computations of currents will be studied. A simple calibration of current with one coefficient by current. A second method where currents are determined by using the Fourier series over the azimuth. The coefficients of this series are then the unknowns of the problem. In this section we will focus on the case of one antenna centered on a 8m-diameter circular ground plane.

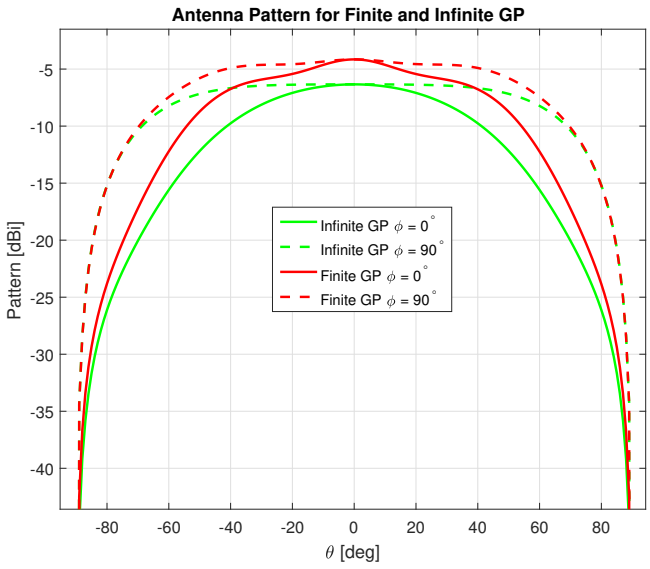


**Figure 4.2:** SKALA antenna pattern centered on an Infinite and Finite GP at 110MHz.

### 4.2.1 Direct current calibration

To minimize the calibration complexity, we must avoid having to many coefficients to determine. A good first set of 72 currents is spread on three circles of 24 currents as displayed on figure 4.3. We can see on this figure the error is higher in the far side lobes. This can be reduced by adding current on further circles.

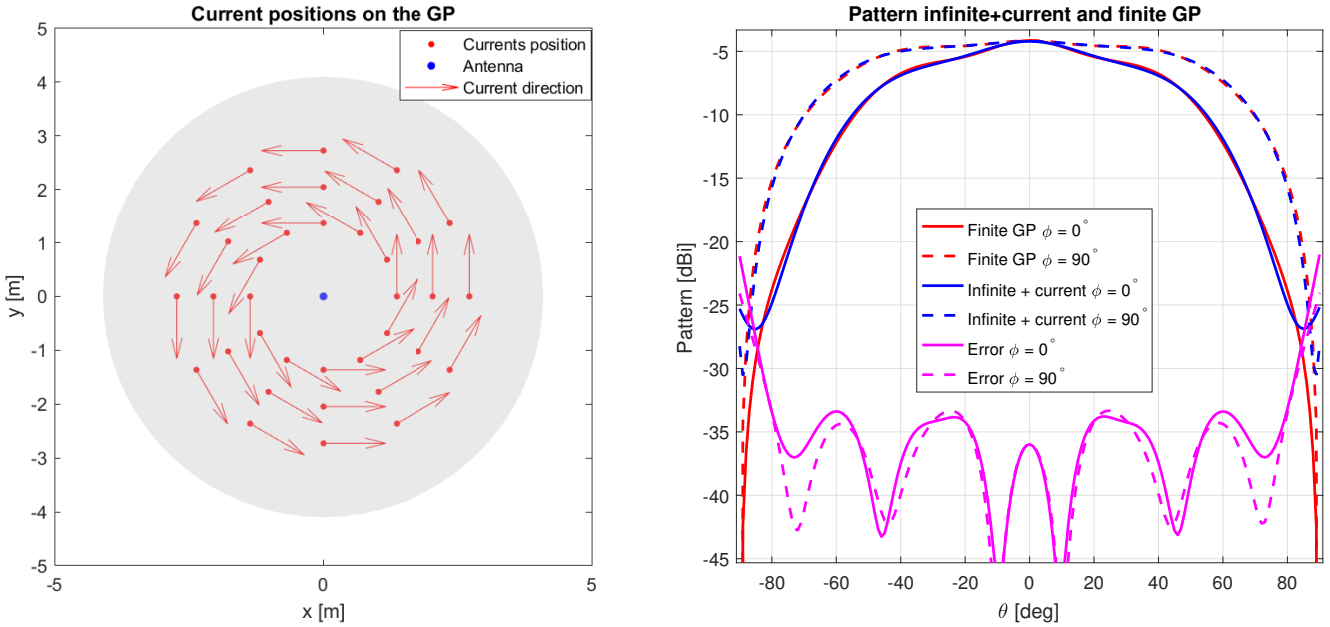


**Figure 4.3:** Positions of currents of the GP (right). Antenna pattern with GP current with infinite GP and finite GP at 110MHz (left)

Contrary to what was expected earlier in Section 4.1, we see in Figure 4.4 that the most important added currents are situated rather near the center of the plane than the perimeter. While adding current to the ground plane, going to 5 circles with 48 currents each, the mean error is reduced from -36.4 dB to -47.82 dB as we can see on the figure 4.3.
We can see the same effect described before with a stronger level, in figure 4.6. Looking more precisely at the center of this distribution, we see that these currents are in fact canceling each other since there are close relatively to the wavelength. This indicates that the solution is mostly mathematical and is certainly relatively far from a physical current distribution.
For an antenna offset by 3 meter on the right direction, we see on figure 4.7 that the finite ground plane simulation with 24 currents per circle does not provide accurate patterns anymore with a mean error of -23.7dB. Nevertheless, increasing the number of currents to 48 per circle allows to reach more reasonable mean error level of -38.7 dB.

### 4.2.2 Fourier series coefficient

To reduce to number of coefficient, a solution is to compute the currents with Fourier series (4.5). This would reduce the number of coefficients per circle from $N_c$ to $N_f$. If the current

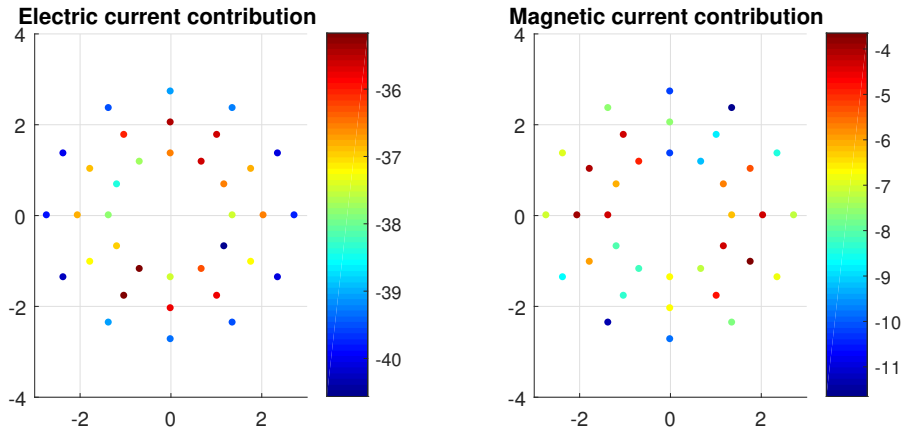


**Figure 4.4:** Norm of the electric and magnetic currents for figure 4.3 according to their position

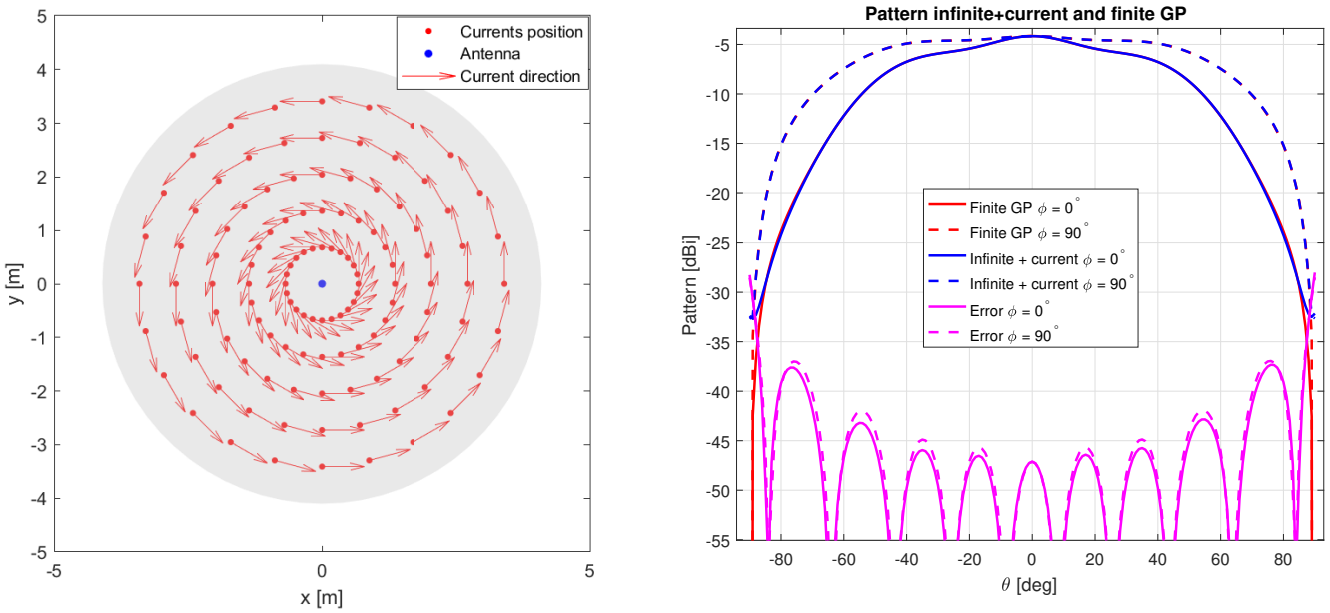


**Figure 4.5:** Positions of currents of the GP (left). Antenna pattern with GP current with infinite GP and finite GP at 110 MHz (right).

distribution along $\phi$ is periodic with a frequency low enough, the number of coefficients for this Fourier series $N_f$ would be low enough to reduce the complexity of the calibration.

$$\alpha_{i_c}(r,\phi) = \sum_{i_f=0}^{N_f} c_{i_f}(r)\ e^{j\ i_f\ \phi} \tag{4.5}$$

Analyzing the value of currents computed with the distribution of figure 4.5, we obtain figure 4.8. We can see that even if the functions are quite near from a sinusoidal, there are points

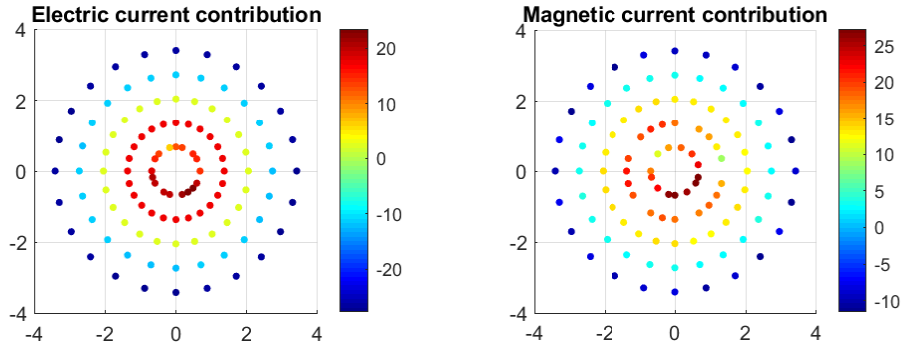


**Figure 4.6:** Norm of the electric and magnetic currents for figure 4.5 according to their position

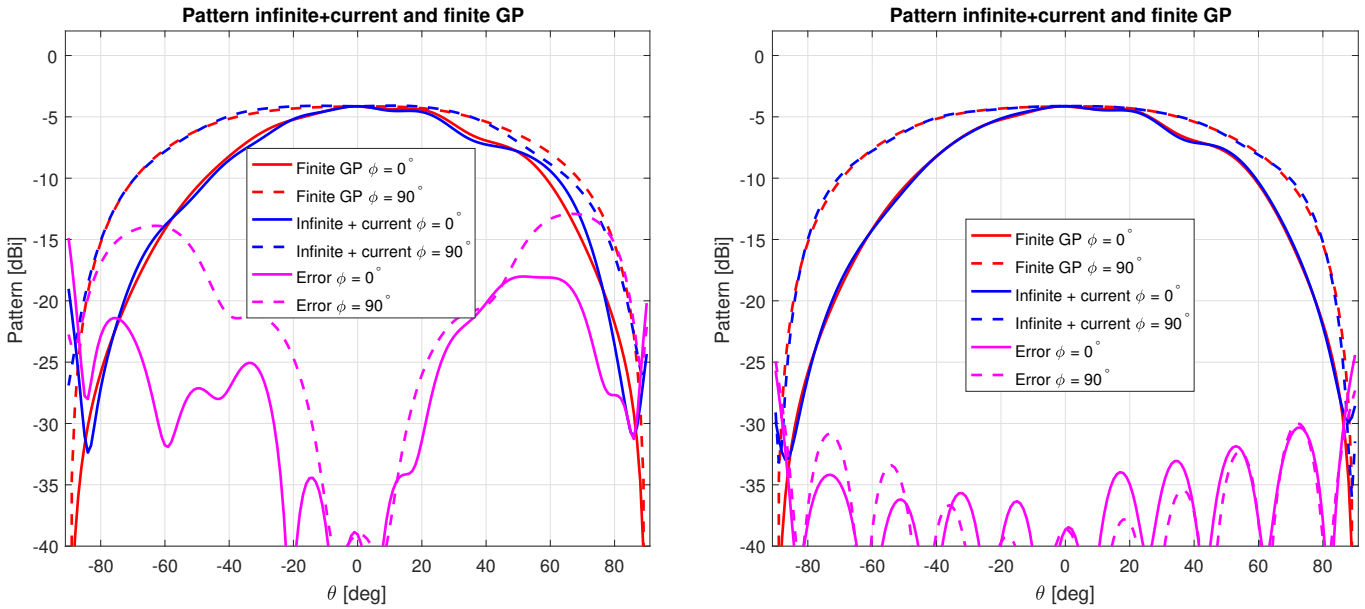


**Figure 4.7:** Antenna pattern with GP current with infinite GP and finite GP at 110MHz for an antenna shifted 3m right using 24x5 currents (left) and 48x5 currents (right).

out of this shape that would require higher frequencies to match and then more Fourier series coefficients. This is mostly the case on the third circle which is one of the most important since the currents are not canceling each other at that distance.

The simulations tell us that the number of currents along $\phi$ don't need to be very high to have a good curve fitting. Then the gain of using the Fourier transformation along this direction loses its interest. At the end, the computation of the coefficients of the Fourier series does not allow one to reduce the size of the least-squares problem.

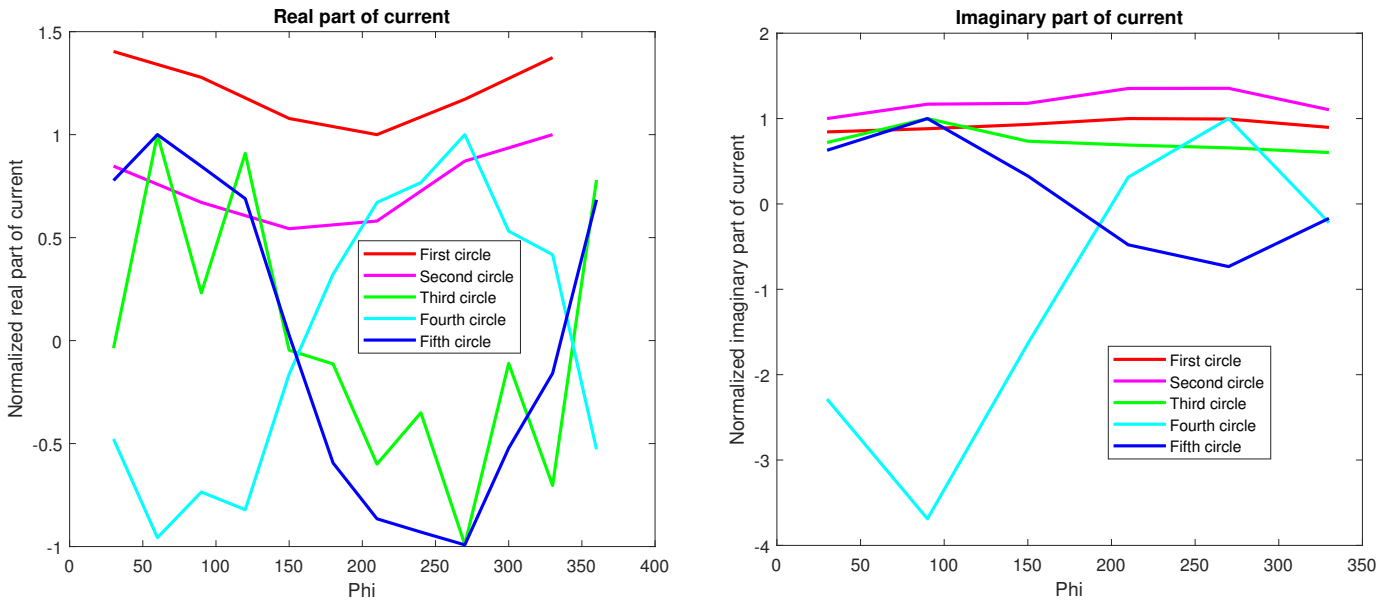


**Figure 4.8:** Normalized representation of the real (left) and imaginary part of electric current on the circles represented in fig. 4.5

## 4.3 Calibration

The representation of the field in Section 4.2, with additional currents on the ground plane, was found using the same problem as a far field calibration of one antenna EEP. The difference is that previously we assumed to know the measurement in each direction of the field and the weight of the antenna itself was fixed to one. The actual calibration only allows a much lower number of experiments or measurement points. We will review the far field and the near field calibration in the same way as we did before with the load impedance effect i.e. starting with far field to have an introduction to what we have to calibrate and if it may work.

### 4.3.1 Far Field

In this chapter, we want to recover the measured EEP from computed EEP with infinite ground plane and ground plane current. The coefficients used to compute the EEP are no more only on other antennas EEP but also on these currents. The problem is a bit change from the set of $N_a$ systems of $N_e$ equations with $N_a$ unknowns (eq. 2.9) described in the section 2.2 to a set of $N_a$ systems of $N_e$ equations with, this time, $N_a + N_c$ unknowns.

The positions of the drone during the calibration are the same described by figure 3.7. Despite using the same path reaching the $\theta = 60°$ directions, the calibration does not achieve to recover the correct coefficients. For an array of 16 antennas, we need to place currents outside of the GP (fig. 4.9) to reach a correct error level of -30 dB.
We can see on figure 4.10, the curve starts to diverge from the correct answer before the 60°.We can may be hope the near field calibration will have better result because it permit to run

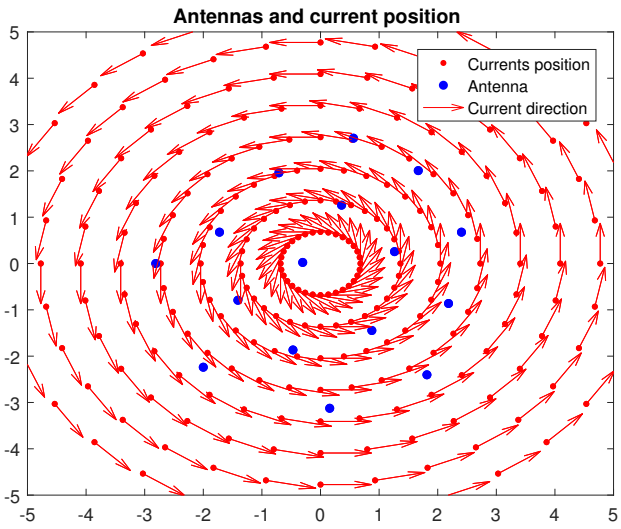


**Figure 4.9:** Positions of the 16 antennas and currents positions

through further viewing angles.

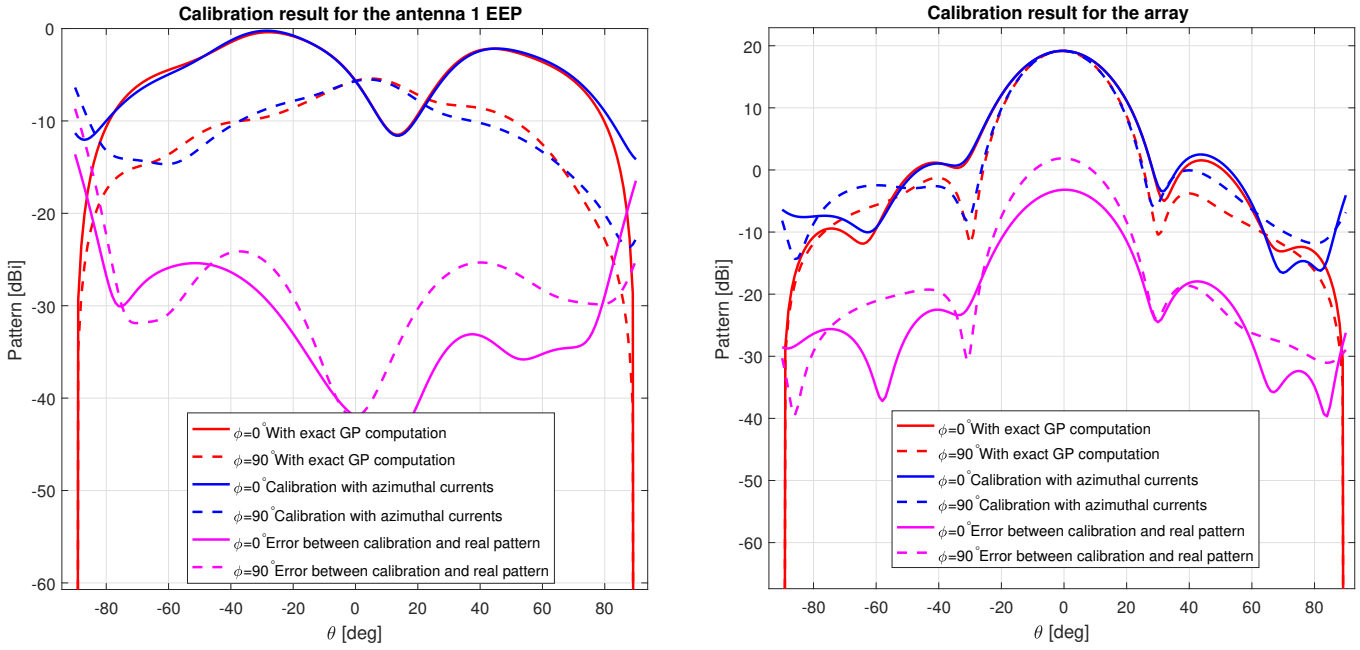


**Figure 4.10:** Results of the calibration of an array of 16 antennas for the EEP of the first antenna (left) the array pattern (right)

Another drawback of this calibration is that the currents of the ground plane take the role of the antennas. It means that the interest of the computation of the infinite GP EEP is reduced since their are finally made by the GP currents.

### 4.3.2 Near Field

We can adapt the expression of the voltage received in near-field 2.11, to add the ground plane currents 4.6.

$$V_k^\tau = \sum_{i=1}^{N_a} \frac{2\lambda Z_L}{j\eta} \sum_{i_m=1}^{N_m} \left( \sum_{i_a=1}^{N_a} \mathbf{p}_{i_m}(\hat{u}_{i_a}) c f^i_{i_m,i_a} c^i_{i_c} \frac{e^{-jkR_{i_a}}}{R_{i_a}} + \sum_{i_c=N_a+1}^{N_a+N_c} \mathbf{G}_{i_c}(\hat{u}_{i_c}) c^i_{i_c} \frac{e^{-jkR_{i_c}}}{R_{i_c}} \right) \cdot \mathbf{F}^d_k(\hat{u}_{i_a})\ V^t_i \tag{4.6}$$

Where the contribution of the point sources $\mathbf{G}_{i_c}(\hat{u}_{i_c})$ and the calibration coefficients $c^i_{1,\dots,(N_a+N_c)}$ are added to the expression. With the measurement points represented in figure 3.9 on the array and currents depicted in figure 4.9, the calibration gives the pattern very different from the original one (figure 4.11).

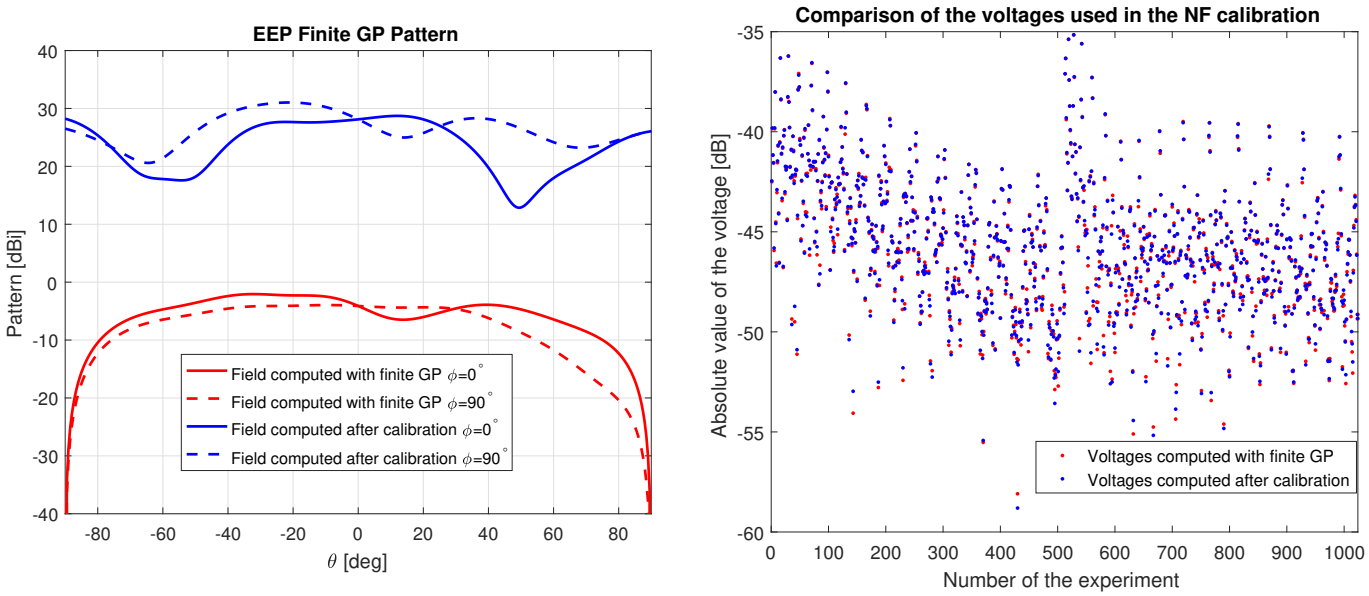


**Figure 4.11:** Results of the NF calibration of an array of 16 antennas for the EEP of the first antenna (left). Comparison of the voltages used in the calibration problem.(right)

We can see that the patterns completely mismatch but the voltages computed with calibration are close from the voltages measured in near-field. The error made by the NF calibration may come from the difference between the solution found by solving the least-squares problem and the physical current distribution. Since the patterns are summing up differently in far-field and near-field, a mathematical solution giving good results for the near field problem may give a wrong estimation in far field.

# Chapter 5

# Conclusion

The calibration of large current array such as the SKA plays an important role in the context of a sensitivity radio telescope. To have the best estimation of the EEP after calibration, we need to have the best model of the system as possible. This Master Thesis reviewed two phenomenons that influence the EEP.

**Load impedance effect:** We have seen that the most important effect comes from the voltage divider made between the antenna and the amplifier. This phenomenon can actually be mostly suppressed by the calibration coefficient of this antenna. A secondary effect slightly changes the shape of the EEPs of the closest antennas, but it needs more degrees of freedom on the calibration to mitigate this effect. At the end, a near-field calibration with noisy UAV positions on an array with varying load impedances, still keeps the error of a below -35 dB.

**Finite ground plane simulation for calibration:** The first part of this section shows the possibility of simulating an antenna on a finite ground plan with a reduced number of currents on the ground plane. Afterwards, the calibration of antennas with their currents has been studied in the far and near field regions. Although the number of currents must be slightly increased, the error in the far-field calibration may stay about -30 dB. However, the solution found is away from the real physical origin of these currents. This difference completely distorts the results find using the near-field calibration leading to incorrect patterns.

# Bibliography


[1] L. van Hoorebeeck, "Calibration of the ska-low antenna array using drones," Master's thesis, June 2018.

[2] G. P. et al., "Medicina array demonstrator: calibration and radiation pattern characterization using a uav-mounted radio-frequency source," *Experimental Astronomy*, vol. 39, pp. 405—421, 2015.

[3] J. Cavillot, "Radiation pattern of the skala antenna in the vicinity of a finite ground plane," Master's thesis, June 2017.

[4] C. A. of Sciences, "Fast radio telescope." http://english.cas.cn/.

[5] N. R. A. Observatory, "Very large array." https://public.nrao.edu/telescopes/vla/.

[6] S. Project, "Ska radio telescope organization." https://www.skatelescope.org.

[7] N. T. N. D. E. de Lera Acedo, N. Razavi-Ghods and A. Faulkner, "Skala, a log-periodic array antenna for ska-low instrument: design, simulations, tests and system considerations," *Experimental Astronomy*, vol. 39.

[8] N. Hexagon positionning intelligence, "An introduction to gnss." https://www.novatel.com/an-introduction-to-gnss.

[9] K. W. Luca Mottola, "A review on array mutual coupling analysis," *Communications of the ACM*, vol. 61, no. 10, pp. 96–104, 2018.

[10] N. R. A. Observatory, "Very large array." https://public.nrao.edu/telescopes/vla/.

[11] J. S. Farnes, "A unifying theory of dark energy and dark matter: Negative masses and matter creation within a modified ACDM framework," *Astronomy  Astrophysics*, no. 620, 2018.

[12] S. Zaroubi, "The Epoch of Reionization," *Astrophysics and Space Science Library*, pp. 45—-101, 2012.

[13] D. G.-O. Christophe Craeye, "A review on array mutual coupling analysis," *Radio science*, vol. 46, 2011.

[14] T. K. Sarkar, A. R. Djordjevic, and B. M. Kolundija, "Method of moments applied to antennas," 2000.

[15] E. d. L. A. Ha Bui-Van, Christophe Craeye, "Fast and accurate simulation technique for large irregular arrays," *IEEE transactions on antennas and propagation*, vol. 66, no. 4, pp. 1805–1817, 2018.

[16] C. L. G. B.Taylor and R. A. Perley, *Synthesis Imaging in Radio Astronomy II*. 1998.

[17] I. A. P. M. Andrea M. Lingua, Marco Piras, "Uav-based pattern measurement of the skala," *IEEE Antennas and Propagation Society International Symposium*, pp. 1372–1373, 2015.

[18] M. S. Neiman, "The principle of reciprocity in antenna theory," *Proceedings of the IRE*, vol. 31, pp. 666–671, 1943.

[19] N. centers for environmental information, "Weather global summary of the year: Meekatharra airport." https://www.ncdc.noaa.gov.

[20] M. I. Patrick Henkel, Ulrich Mittmann, "Real-time kinematic positioning with GPS and GLONASS.," *European Signal Processing Conference (EUSIPCO)*, vol. 24, pp. 1063–1067, 2016.

[21] C. Craeye, "Pattern transformation in arrays of multi-mode antennas," *Université Catholique de Louvain, internal document*, June 2018.

**UNIVERSITÉ CATHOLIQUE DE LOUVAIN**
**École polytechnique de Louvain**
Rue Archimède, 1 bte L6.11.01, 1348 Louvain-la-Neuve, Belgique | **www.uclouvain.be/epl**